

The MIDAS telescope for microwave detection of ultra-high energy cosmic rays

J. Alvarez-Muñiz^a, E. Amaral Soares^b, A. Berlin^c, M. Bogdan^c, M. Boháčová^{c,d}, C. Bonifazi^b,
W. R. Carvalho Jr.^a, J. R. T. de Mello Neto^b, P. Facal San Luis^c, J. F. Genat^c, N. Hollon^c, E. Mills^c,
M. Monasor^c, P. Privitera^c, A. Ramos de Castro^b, L. C. Reyes^{c,e}, B. Rouille d'Orfeuil^c, E. M. Santos^b,
S. Wayne^c, C. Williams^c, E. Zas^c, J. Zhou^c

^aUniversidad de Santiago de Compostela, Departamento de Física de Partículas,
Campus Sur, Universidad, E-15782 Santiago de Compostela, Spain

^bUniversidade Federal do Rio de Janeiro, Instituto de Física,
Cidade Universitaria, Caixa Postal 68528, 21945-970 Rio de Janeiro, RJ, Brazil

^cUniversity of Chicago, Enrico Fermi Institute & Kavli Institute for Cosmological Physics,
5640 S. Ellis Ave., Chicago, IL 60637, USA

^dInstitute of Physics of the Academy of Sciences of the Czech Republic,
Na Slovance 2, CZ-182 21 Praha 8, Czech Republic

^eDepartment of Physics, California Polytechnic State University, San Luis Obispo, CA 93401, USA

Abstract

We present the design, implementation and data taking performance of the MICrowave Detection of Air Showers (MIDAS) experiment, a large field of view imaging telescope designed to detect microwave radiation from extensive air showers induced by ultra-high energy cosmic rays. This novel technique may bring a tenfold increase in detector duty cycle when compared to the standard fluorescence technique based on detection of ultraviolet photons. The MIDAS telescope consists of a 4.5 m diameter dish with a 53-pixel receiver camera, instrumented with feed horns operating in the commercial extended C-Band (3.4 – 4.2 GHz). A self-trigger capability is implemented in the digital electronics. The main objectives of this first prototype of the MIDAS telescope - to validate the telescope design, and to demonstrate a large detector duty cycle - were successfully accomplished in a dedicated data taking run at the University of Chicago campus prior to installation at the Pierre Auger Observatory.

1. Introduction

The origin and composition of Ultra-High Energy Cosmic Rays (UHECRs) remains uncertain [1], even after the progress made by the latest generation of experiments [2, 3]. Due to the strong flux suppression above 10^{19} eV [4, 5], very large detection areas are necessary to study cosmic rays at these energies. A future UHECR Observatory based on standard techniques - Surface Detector arrays (SD) and Fluorescence Detectors (FD) - may be limited by cost and difficulty of deployment. In this context, radio detection techniques are attractive thanks to the low cost of individual elements, the little maintenance required and a nearly 100% detection duty cycle.

Radio emission in the MHz range from extensive air showers (EAS) has been actively studied in the

last decade by the LOPES [6] and CODALEMA [7] experiments. MHz radio-detection is now well established, and AERA [8], in commissioning phase at the Pierre Auger Observatory, will have a sufficiently large instrumented area to explore the potential of this technique for detection of the highest energy cosmic rays.

The use of the microwave (GHz) band for EAS detection was originally pursued by Jelley, Charman and collaborators [9, 10] in the late 1960s, but abandoned due to the lack of satisfactory understanding of the emission mechanisms and to limitations in detector technology. Thereafter it remained mostly unexplored, until recent laboratory measurements [11] with particle beams have renewed the interest in this part of the radio spectrum. These measurements suggest that microwave radiation is emitted from the weakly ionized air



Figure 1: The MIDAS telescope at the University of Chicago, with the 53-pixel camera at the prime focus of the 4.5 m diameter parabolic dish reflector.

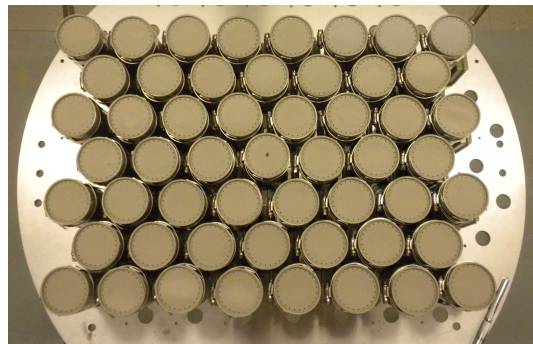


Figure 2: A front view of the receiver camera, with LNBFs closely packed to maximize the sensitivity over the focal plane.

36 plasma of free electrons produced by the EAS induced
 37 ionization of the atmosphere. The radiation
 38 is expected to be continuous and relatively flat
 39 in frequency, unpolarized and emitted isotropically,
 40 and its intensity to scale with the number of particles
 41 of the shower.

42 Detection of an isotropic emission in the GHz
 43 range - akin to the detection of ultraviolet fluorescence
 44 photons by FD pioneered by the Fly's Eye experiment [12]
 45 and currently used by the Pierre Auger Observatory [13]
 46 and the Telescope Array [14] - allows for the measurement
 47 of the EAS development in the atmosphere, which provides
 48 a calorimetric measurement of the energy and crucial
 49 information on the mass composition of primary cosmic
 50 rays. A GHz radio telescope would overcome the limitations
 51 of the FD technique, i.e. data taking only during moonless
 52 nights ($\approx 15\%$ duty cycle) and significant systematic
 53 uncertainties introduced by light attenuation in the atmosphere.
 54 In fact, microwave detectors can operate 100% of the
 55 time, and attenuation in the GHz range is minimal,
 56 even with rain or clouds. Moreover, commercial off-the-shelf
 57 GHz equipment, mostly developed for satellite TV reception,
 58 is readily available and inexpensive. Microwave telescopes
 59 could provide ex-

62 isting UHECR experiments of unprecedented sensitivity
 63 to primary cosmic ray composition, and be employed
 64 in a future large scale observatory.

65 Several complementary approaches to microwave
 66 detection of EAS are currently being pursued, including
 67 the AMBER and EASIER detectors [15] at the Pierre Auger
 68 Observatory, and the CROME experiment at KASCADE [16].
 69 Also, new laboratory measurements with particle beams
 70 are being performed [17, 18] to better characterize the
 71 microwave emission.

72 In this paper, we present the MICrowave Detection
 73 of Air Showers (MIDAS) experiment, an imaging telescope
 74 whose primary objective is to confirm the microwave
 75 emission from EAS, and to demonstrate the feasibility
 76 of a low cost design for this novel technique. The MIDAS
 77 telescope is described in Sec. 2. The electromagnetic
 78 simulations of the telescope response are illustrated in
 79 Sec. 3. The calibration procedures and the measured
 80 sensitivity of the instrument are presented in Sec. 4. A
 81 realistic simulation of the MIDAS detection of EAS is
 82 described in Sec. 5. Operation and data taking
 83 performance of the MIDAS telescope are presented in
 84 Sec. 6, and conclusions are drawn in Sec. 7.

87 2. The MIDAS telescope

88 The telescope consists of a large parabolic dish
 89 reflector with a receiver camera at its prime focus,
 90 installed on the roof of the Kersten Physics Teaching
 91 Center at the University of Chicago (Fig. 1). In the
 92 following, the design and technical implementation of
 93 the different components of the MIDAS telescope are
 94 described.

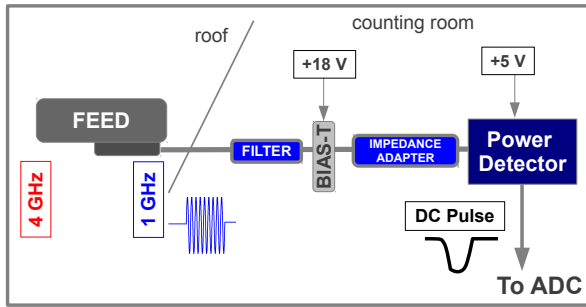


Figure 3: The analog electronics chain. See text for details on the different components.

2.1. Reflector and receiver camera

The parabolic dish reflector (Andrew) has 4.5 m diameter and $f/D = 0.34$. A motorized alt-azimuth mount allows for telescope movements in a range of 90° in elevation and 120° in azimuth. The remote control of the telescope pointing (0.1° precision) is integrated in the data acquisition (DAQ) system (Sec. 2.5). A 53-pixel receiver camera is mounted on the prime focus of the dish, covering a field of view of about $20^\circ \times 10^\circ$. The microwave receivers are arranged in seven rows, and staggered to maximize the sensitivity across the focal plane (Fig. 2).

A commercial low noise block feed horn (LNBF) operating in the extended C-band (3.4 - 4.2 GHz) is used for the receiver. These feeds (WS International) are mass-produced for consumer satellite television. The LNBF integrates a feed horn, low noise amplifiers, and a frequency downconverter. The feed can receive two orthogonal linear polarizations which are remotely selectable through the LNBF power voltage level setting. A 5150 MHz local oscillator in the frequency downconverter mixes the input RF signal down to a frequency interval of 950-1750 MHz, which is transmitted with minimal loss through standard coaxial cable. The receiver bandwidth, its gain Γ and noise temperature were measured to be about 1 GHz, 65 dB and 20 K, respectively.

Power to the LNBF is provided through 30 meters of commercial quad-shielded RG-6 coaxial cable, which also brings the RF signal, after amplification and downconversion, from the telescope to the counting room.

2.2. Analog electronics

The analog electronics chain is summarized in Fig. 3. The RF signal in the coaxial cable is first

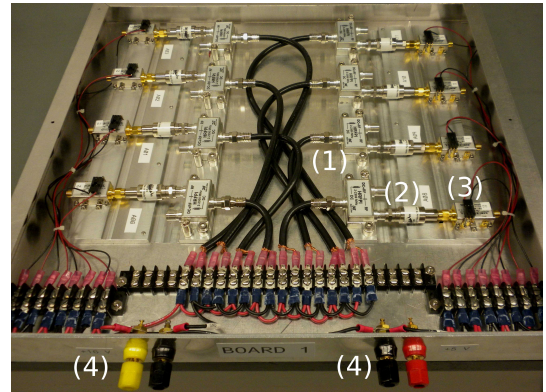


Figure 4: An analog electronics tray with eight channels. The bias tee (1), impedance adapter (2), power detector (3), and DC voltage inputs (4) are visible.

passed through a bandpass filter (1.05-1.75 GHz). The purpose of the filter is to reject interference from radar altimeters of airplanes, which was identified as a major source of background in the early stage of commissioning of the telescope. A power inserter (commonly called bias tee) provides the DC voltage to the LNBF, while letting through the RF signal. An impedance adapter matches the standard 75 Ohm impedance of these commercial satellite TV components to the 50 Ohm impedance of the RF power detector (Mini-Circuits ZX47-60-S+). The overall power loss L in the 30 m of cable and in the analog electronics was measured to be 17 dB.

The power detector (input bandwidth ≈ 8 GHz) responds logarithmically to an RF power P in the range -55 dBm to 5 dBm, with a voltage output between 2.0 V and 0.5 V:

$$V = V_0 - 10 a \log(P), \quad (1)$$

with P in mW. The characteristics of the 53 power detectors were individually measured, with typical values around $V_0 = 0.625$ V and $a = 0.025$ V/dB. Also, their response time was found to be about 100 ns, well suited for typical pulses of microseconds duration expected from an EAS crossing the field of view of a pixel.

The analog electronics components are arranged in trays - 8 channels per tray - for distribution of DC power and routing of the signals to the digital electronics (Fig. 4).

2.3. Front-End electronics and digitizers

The signal from the power detector is digitized with 14-bit resolution (calibration constant

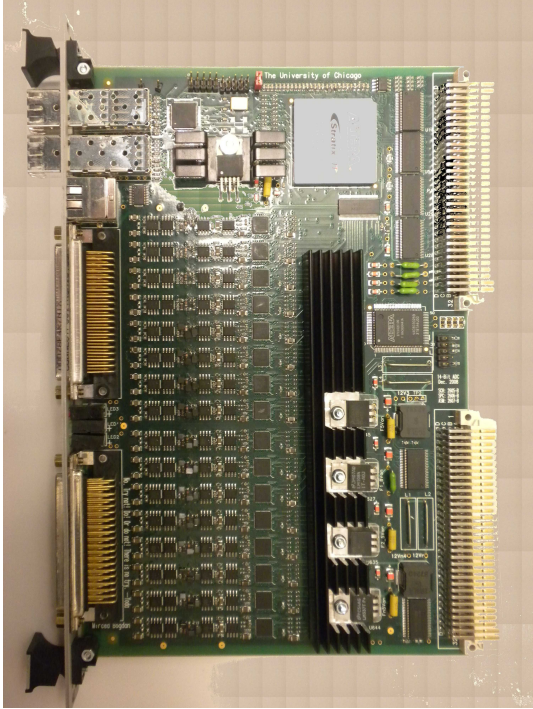


Figure 5: Digital electronics board with 16 Flash-ADC channels. The module includes an FPGA for the First Level Trigger logic and a VME interface. The board was designed by the Electronics Design Group at the Enrico Fermi Institute of the University of Chicago.

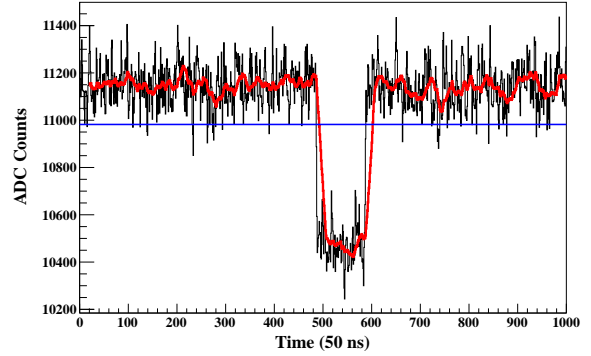


Figure 6: Illustration of the FLT. The digitized time trace for a $5 \mu\text{s}$ RF pulse from the calibration antenna (see Sec. 2.5), with the ADC running average of 20 consecutive time samples superimposed as a gray histogram (red in the color version). An FLT is issued when the running average falls below the threshold, indicated by the horizontal line.

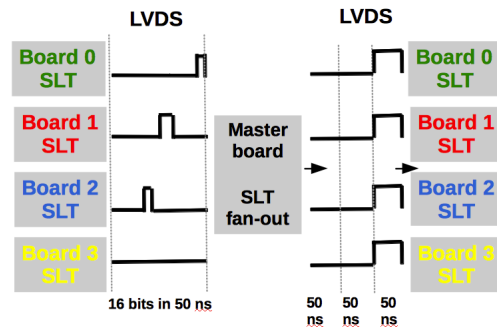
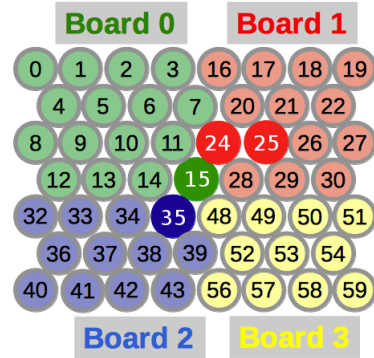


Figure 7: Illustration of the SLT. The 4 highlighted pixels (top panel), located in three different FADC boards, have an FLT occurring in the same 50 ns time sample. Each FADC board sends through the LVDS lines the FLT status of its pixels to the Master Trigger Board (bottom panel, left), where a matching SLT pattern is found. An SLT is then sent back through the LVDS lines to the FADC boards (bottom panel, right) triggering the entire camera for data readout.

164 $b = 7 \text{ ADC/mV}$) at a sampling rate of 20 MHz by
 165 custom-made Flash-ADC (FADC) boards (Fig. 5).
 166 Up to 2048 samples are stored in a circular buffer
 167 and processed by a first level trigger algorithm
 168 implemented in the on-board FPGA. A standard
 169 VME interface allows for board control and data
 170 readout.

171 Four FADC boards, each with 16 channels, are
 172 sufficient for the entire receiver camera. A Master
 173 Trigger Board, also equipped with FPGA logic and
 174 VME interface, provides the global clock for the
 175 FADC synchronization and performs a high level
 176 trigger decision. Each FADC board is connected to
 177 the Master Trigger board through Low Voltage Dif-
 178 ferential Signaling (LVDS) lines carrying the clock
 179 and trigger signals.

180 A VME module equipped with a GPS receiver
 181 (Hytec 2092) tags the time of the triggered events
 182 with 10 ns precision. Details of the MIDAS digital
 183 electronics can be found in [19].

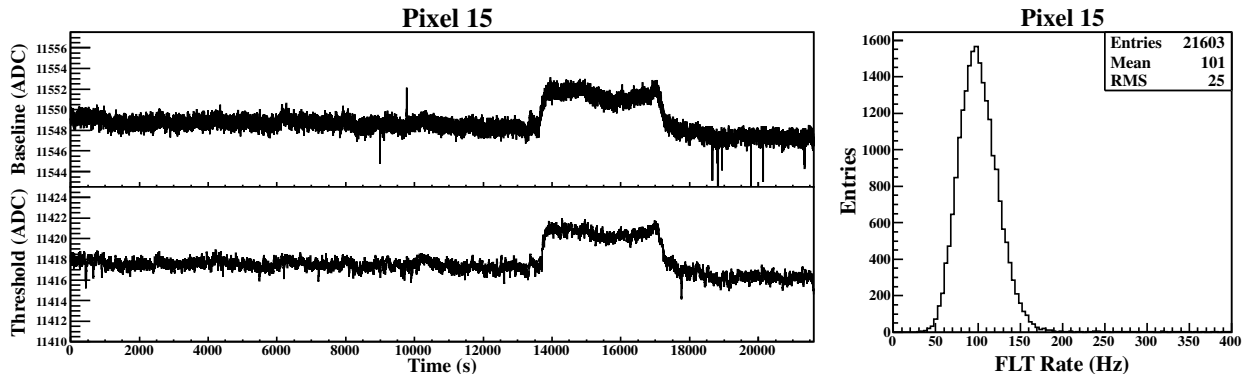


Figure 8: Monitoring data from one pixel for a six-hour data taking run. On the left, the ADC baseline averaged over 10 ms (upper panel) and the FLT threshold (bottom panel) as a function of time. The threshold follows closely the variations of the baseline, keeping the FLT rate during the run (right panel) around 100 Hz.

2.4. Trigger

MIDAS implements a multi-level trigger architecture, optimized for transient events with topology and time structure compatible with signals from an EAS. The system is modeled on the one successfully operating at the FD of the Pierre Auger Observatory [13]. For each channel, a First Level Trigger (FLT) algorithm identifies pulses in the FADC trace. The FLT information from all channels is sent to the Master Trigger Board where the Second Level Trigger (SLT) searches for patterns of FLT's compatible with a cosmic ray track.

The FLT status bit of a given channel is activated whenever the ADC running sum of 20 consecutive time samples falls below a threshold (Fig. 6). To compensate for changes in the noise level, the threshold is continuously regulated in order to keep a stable FLT rate around 100 Hz. The active status of the FLT bit is extended for 10 μ s after the trigger, to allow for time coincidences between different channels in the Master Trigger Board.

Every 50 ns, each FADC board transmits 16 bits, corresponding to the FLT status of its 16 channels, to the Master Trigger Board (Fig. 7), where the SLT trigger algorithm searches for 4-fold patterns of channels with FLT triggers overlapping in time. There are 767 patterns compatible with the topology of a cosmic ray shower (straight tracks across the camera). When an SLT matching pattern is found, an event trigger signal is distributed back to the FADC boards and to the GPS module. At this point, a block of 100 μ s of ADC data (including 500 pre-trigger samples) is frozen in the memory buffer and made available for readout via VME. All 53

channels, even those not participating to the trigger decision, are readout.

Higher levels of trigger control have also been implemented. For example, the FLT threshold regulation and data acquisition are inhibited whenever the SLT rate is higher than a certain limit, to be automatically restored when the SLT rate comes back to a normal level.

2.5. Data acquisition, monitoring and operation

A single board computer (GE Intelligent Platforms V7865) acting as VME master is used for the data acquisition. The DAQ software monitors the relevant VME registers of the FADC boards, and reads out through the VME bus the GPS time stamp and the data available in the buffer after an event trigger. The event data are then assembled and written to disk in ROOT format [20].

For monitoring purposes, the ADC baseline averaged over 10 ms (calculated in the FPGA of the FADC board), the FLT rate, and the FLT threshold of each channel are readout and recorded every second. An example of monitoring data collected during a six-hour data taking run is presented in Fig. 8.

Additional monitoring information is obtained from RF pulses periodically illuminating the receiver camera. For this purpose, a patch antenna with a wide beam (HPBW=70°) is mounted at the center of the reflector dish. The antenna is driven by an RF signal generator located in the counting room, which every 15 minutes produces a train of ten RF pulses of 10 μ s width. These data provide monitoring information for all of the channels at

the same time, ensuring they are properly operating and that the trigger is working as designed.

Data runs last six hours and are automatically restarted, with data files backed up on a server for offline analysis. A fully automatic and remote operation of the telescope was achieved through a slow control software for the antenna positioning, and for the status of power supplies and of the VME crate.

3. EM simulation of telescope efficiency

The efficiency of the MIDAS telescope has a significant angular dependence, due to the large field of view implemented in a parabolic reflector. For a proper calibration of the telescope and for a realistic estimate of its sensitivity to EAS, the power pattern of each pixel - i.e the pixel detection efficiency as a function of the direction (θ, ϕ) of the incident microwave radiation with respect to the telescope boresight - must be determined. A full electromagnetic (EM) simulation of the reflector and receiver camera has been developed for this purpose.

At radio and microwave wavelengths, it is convenient to simulate the antenna system (reflector and feed) in emission mode, making use of the so-called Reciprocity Theorem [21, 22] to obtain its effective area A_i in a given direction:

$$A_i(\theta, \phi) = \frac{\lambda^2}{4\pi} G_i(\theta, \phi), \quad (2)$$

where λ is the wavelength of the radiation and $G_i(\theta, \phi)$ is the gain of the antenna system for pixel i , defined as the power emitted per unit solid angle in the direction (θ, ϕ) normalized to the corresponding power emitted by an isotropic radiator. In practical terms, the antenna effective area summarizes the dependence of the telescope gain on the dimensions of the reflector, the frequency of the radiation, and overall illumination (i.e. taper) of the feed.

The feed is simulated as two cylindrical waveguides - the one corresponding to the feed aperture having a diameter $d = 6.7$ cm and the other having a diameter $d = 5.5$ cm - joined by a small conical throat. The dominant propagating mode is the TE_{11} (electric field perpendicular to the feed axis) with a cutoff wavelength of 9.4 cm determined by the diameter of the end section ($\lambda_{TE_{11}}^c = 1.71d$) [23]. The calculated radiation pattern of the feed in

polar coordinates for the E-plane ($\phi = \pi/2$) and H-plane ($\phi = 0$), and the direction of the electric vector field over the feed aperture are shown in Fig. 9.

To obtain the antenna effective area, the electromagnetic field distribution over the telescope aperture is calculated. For each feed, the telescope aperture is found by intersection of rays emitted by the feed with the plane perpendicular to the telescope axis and containing the dish focal point. The paths of rays from the feed to the aperture plane are determined in the optical limit using Fermat's principle of least transit time. Spherical wave propagation is assumed from feed to dish and plane wave propagation is assumed from dish to aperture. A proper treatment of the optical paths is essential for MIDAS, since the lateral displacement of the feeds with respect to the dish focal point produces significant differences in their gain. Also, the shadow of the receiver camera, which increases the size of sidelobes, is included in the simulation. The radiation field is then calculated in the far-field limit by the Fourier transform of the aperture field distribution, and the power is obtained as the square of the associated Poynting vector.

Equation 2 holds for an antenna system completely matched to its transmission line. In practice, reflections at the feed entrance, at the throat between the cylindrical sections and at the coupling between the feed and the coaxial line reduce the antenna effective area. Their effect can be calculated introducing an equivalent transmission line model with impedance mismatches which produce reflected power waves. Additional signal losses in the coaxial cable and in the analog electronics are included in the simulation. Also, the reflector does not collect all the power emitted by the feed, and part of it spills over, further reducing the antenna total effective area.

The result of the EM simulation can be expressed as a relative power pattern for each pixel i :

$$\epsilon_i(\theta, \phi) = \frac{G_i(\theta, \phi)}{G_{15}(0, 0)}, \quad (3)$$

where $G_{15}(0, 0)$ is the calculated gain of the central pixel in the direction of boresight. The pattern for the central feed (Fig. 10, left) is symmetric around the boresight with relatively small sidelobes. Feeds away from the focal point (Fig. 10, right) have smaller gains and bigger, asymmetrical lobes. From Eq. 2, the effective area of the antenna system to a microwave flux incident from a given direction is

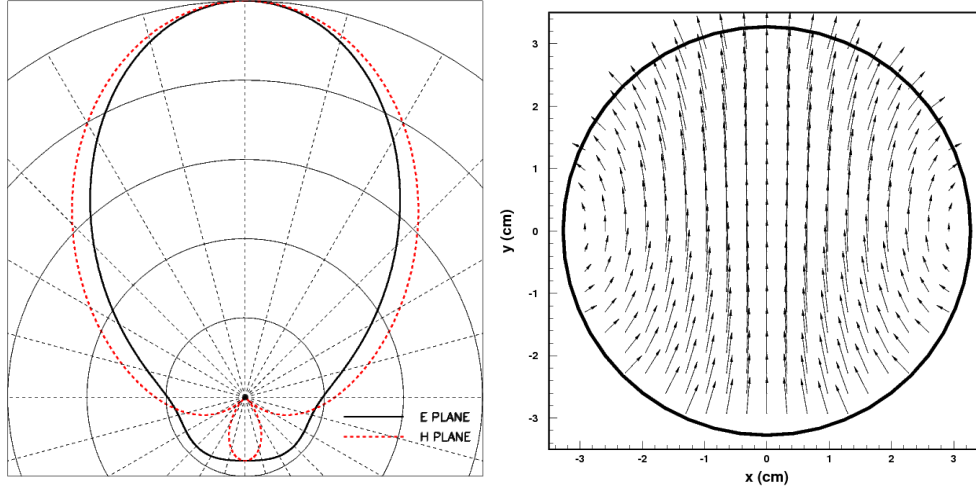


Figure 9: EM calculation of the feed for the dominant TE₁₁ mode at 3.8 GHz. Left: Normalized electric field radiation pattern for the MIDAS feed in polar coordinates. Both the E-plane ($\phi = \pi/2$) and H-plane are shown ($\phi = 0$). Right: Electric field vector over the feed aperture.

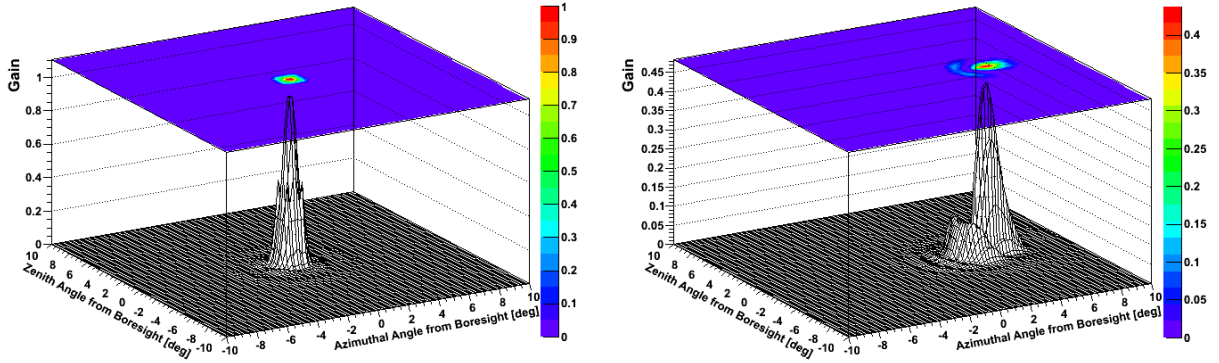


Figure 10: Left: Power radiation pattern for the central feed (pixel 15) of the MIDAS camera. This feed presents the maximum antenna gain of the receiver camera, and a symmetrical pattern with very small sidelobes. Right: Radiation pattern for a feed laterally displaced by 16.5 cm ($\sim 2\lambda$) from the camera focus (pixel 13). Its gain is $\sim 50\%$ smaller, and presents a significant coma lobe.

346 then given by:

$$347 \quad A_i(\theta, \phi) = A_{eff} \epsilon_i(\theta, \phi), \quad (4)$$

348 where $A_{eff} = \frac{\lambda^2}{4\pi} G_{15}(0,0)$ is the effective area of
349 the dish.

350 The overall sensitivity of the camera can be
351 calculated summing over the pixels: $\epsilon(\theta, \phi) =$
352 $\sum_i \epsilon_i(\theta, \phi)$, and is presented in Fig. 11. Even with
353 the compact arrangement of the MIDAS feeds over
354 the focal plane, there is a region of reduced effi-
355 ciency between adjacent feeds. Also, the efficiency
356 at the borders of the field of view is as low as 20% of
357 the efficiency at the center. While not uniform over

358 the camera, the telescope efficiency is reasonably
359 high in a large portion of its field of view, which is
360 sufficient for the goals of this first low-cost proto-
361 type for the MIDAS concept.

362 4. Telescope Calibration

Dedicated calibration measurements were per-
formed during the commissioning of the telescope,
which were followed up during data taking to verify
the stability of the system.

The Sun, whose flux in the microwave range is
measured daily by several solar radio observato-

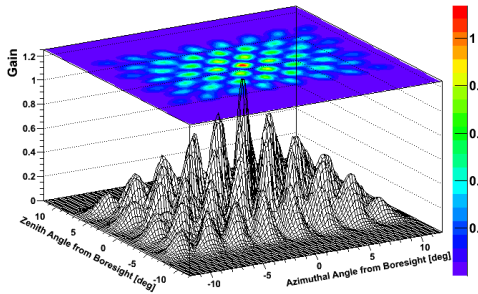


Figure 11: Radiation pattern of the MIDAS camera, calculated by summing over all pixels, as function of the angle with respect to the antenna boresight.

369 ries around the world, was used as the primary
 370 source for the absolute calibration of the MIDAS
 371 telescope. This calibration was cross-checked with
 372 other known astrophysical sources.

373 The monitoring patch antenna (Sec. 2.5) was also
 374 used for relative channel calibration.

375 4.1. Absolute calibration

376 An unpolarized microwave flux density, F , inci-
 377 dent on the MIDAS reflector from a direction (θ, ϕ)
 378 produces, at the input of the power detector of a
 379 given pixel i , a power P_i given by:

$$\begin{aligned} P_i &= \frac{L_i \cdot \Gamma_i \cdot B_i \cdot A_{eff} \cdot \epsilon_i(\theta, \phi) \cdot F}{2} \\ &= \alpha_i \cdot \epsilon_i(\theta, \phi) \cdot F, \end{aligned} \quad (5)$$

380 where $\epsilon_i(\theta, \phi)$ is the pixel relative power pattern,
 381 A_{eff} is the effective area of the dish, B_i is the
 382 bandwidth of the electronics (essentially given by
 383 the pixel bandpass filter), Γ_i is the gain of the re-
 384 ceiver, L_i is the loss due to the 30 m cable and the
 385 analog electronics, and the factor 2 takes into ac-
 386 count the fact that the linearly polarized receivers
 387 detect only half of the available power. The output
 388 voltage of the power detector (Eq. 1) is digitally
 389 sampled in the FADC board, yielding a signal n_i in
 390 ADC counts:

$$n_i = n_i^0 - 10 k_i \log [\alpha_i \cdot \epsilon_i(\theta, \phi) \cdot F], \quad (6)$$

392 where $n_i^0 = bV_0$, and $k_i = ab \simeq 175$ ADC/dB with
 393 a , V_0 and b as defined in Sec. 2.2 and 2.3, respec-
 394 tively. The calibration constant k_i is independently
 395 measured for each channel (see Sec. 4.2).

396 Even when the telescope is pointed towards a re-
 397 gion of the sky with no microwave sources, a power

398 P_i^{sys} is present at the input of the power detector,
 399 with a corresponding signal n_i^{sys} in ADC counts.
 400 Sources for this signal include radiation from the
 401 sky in the main beam of the antenna, radiation
 402 from ground in the antenna sidelobes, and electron-
 403 ics noise, dominated by the receiver noise temper-
 404 ature. An equivalent flux density, F_i^{sys} , is defined
 405 from $P_i^{sys} = \alpha_i F_i^{sys}$.

406 A measured signal n_i can be converted into an ab-
 407 solutely calibrated flux density F by deriving from
 408 Eq. 6:

$$n_i = n_i^{sys} - 10 k_i \log \left(1 + \frac{\epsilon_i(\theta, \phi) \cdot F}{F_i^{sys}} \right), \quad (7)$$

410 where $\epsilon_i(\theta, \phi)$ is taken from the simulation de-
 411 scribed in Sec. 3, and n_i^{sys} and the corresponding
 412 F_i^{sys} must be determined through calibration pro-
 413 cedures.

414 The Sun was used as the main calibration source
 415 of the MIDAS telescope, by measuring the pixel
 416 signal during a transit of the Sun in its field of view.
 417 From Eq. 7, the time evolution of the signal is given
 418 by:

$$n_i(t) = n_i^{sys} - 10 k_i \log \left(1 + \frac{\epsilon_i(\theta(t), \phi(t)) \cdot F_{sun}}{F_i^{sys}} \right), \quad (8)$$

419 where n_i^{sys} is the ADC baseline measured before the
 420 Sun transit, $(\theta(t), \phi(t))$ is the sun position in the sky
 421 at time t , and the Sun flux density, F_{Sun} , is taken
 422 from the daily measurements by the Nobeyama ob-
 423 servatory [24]. The value of F_i^{sys} which best de-
 424 scribe the calibration data is then obtained. An
 425 extensive measurement campaign was performed,
 426 with each Sun transit aiming to the calibration of
 427 a row of pixels. An example of a Sun calibra-
 428 tion run for the top row of pixels is presented in
 429 Fig. 12. These measurements not only provide an
 430 absolute calibration of each pixel through F_i^{sys} , but
 431 also demonstrate the quality of the simulation of
 432 $\epsilon_i(\theta, \phi)$. In fact, simulations were found to describe
 433 very well the pixel power pattern in both the width
 434 and the relative efficiency of the lobes, even for pix-
 435 els at the edges of the camera where strong aberrations
 are present.

As an example, several calibration measurements
 of the central pixel yielded a $F_{15}^{sys} = 1.96 \cdot 10^4$ Jy*,

*1 Jy = 10^{-26} W/m²/Hz

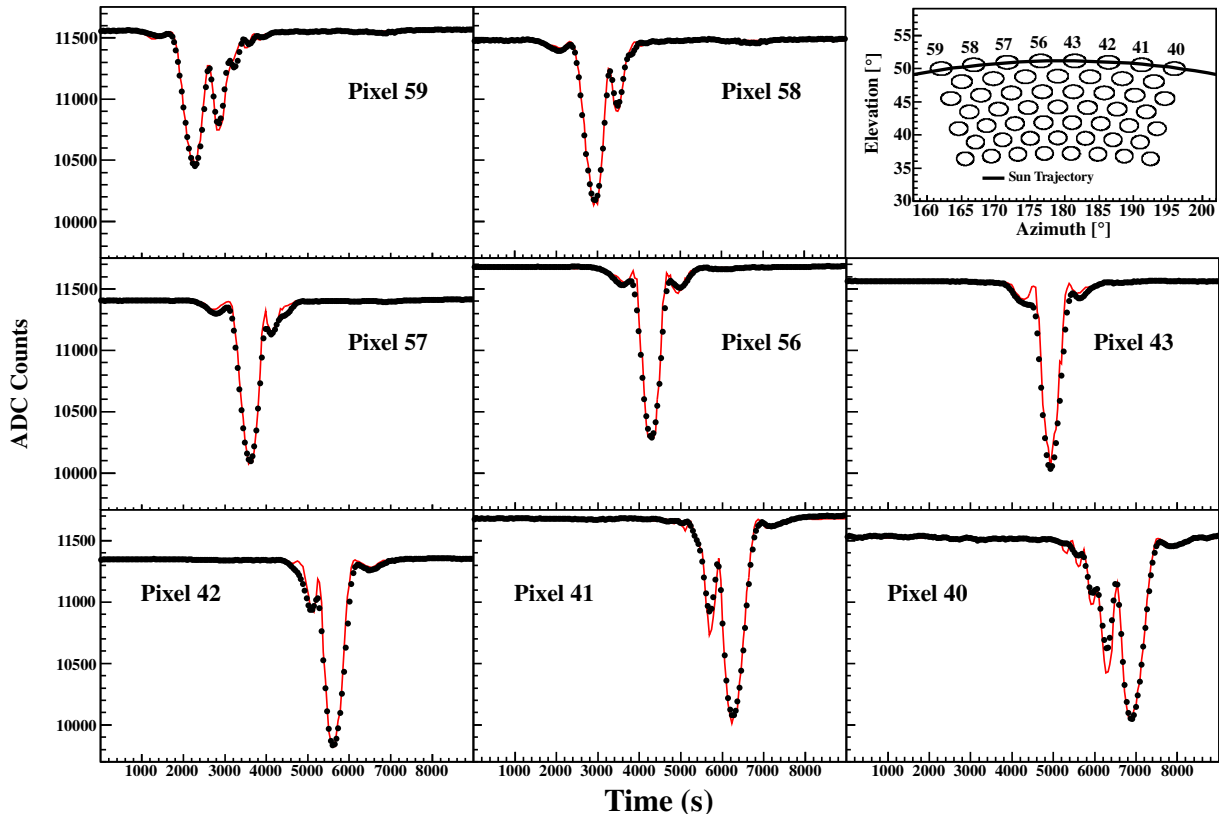


Figure 12: Example of a calibration measurement of the MIDAS telescope with a Sun transit. Top right inset: Sun trajectory in the top row of the camera pixels (azimuth measured clockwise from North). The measured ADC signal (closed dots) for each pixel is shown in the other panels, with the superimposed line representing the EM simulation for the best value of F_i^{sys} (see text).

equivalent, in the common notation of radio astronomy, to a system temperature T_{sys} of:

$$T_{sys} = \frac{F_{15}^{sys} \cdot A_{eff}}{2k_b} = 65 \text{ K}, \quad (9)$$

where k_b is the Boltzmann constant, and $A_{eff} = 9.1 \text{ m}^2$ is the effective area ($\approx 60\%$ of the geometric area) of the telescope as determined by simulations described in Sec. 3. The other pixels had a similar system temperature. The estimated systematic uncertainty on the measurement of F_i^{sys} is 15%, dominated by the uncertainty of the Nobeyama measurement and of the telescope pointing.

Measurements of the Moon ($F_{Moon} \simeq F_{Sun}/100$) and of the Crab Nebula ($F_{Crab} \simeq F_{Sun}/1000$) were also performed, providing a cross-check of the absolute calibration. Using the Sun calibration, the Moon temperature was found to be 245 K, to be compared with 268 K [25] (the measurement was taken a day after the full moon). The flux density

of the Crab Nebula was measured to be 760 Jy, to be compared with 718 ± 43 Jy at 3.38 GHz [26]. Both of these results agree to better than 10%, within the estimated systematic uncertainty of the Sun calibration.

4.2. Pixel calibration constants and timing

The calibration constant k_i in Eq. 6 was measured by using the patch antenna mounted at the center of the dish. The pulse power P_{pulse} of the RF signal generator driving the patch antenna was changed over a wide range, and the corresponding signal n_i^{pulse} was measured for each channel. From Eq. 7, one expects:

$$n_i^{pulse} = n_i^{sys} - 10 k_i \log \left(1 + \frac{f_i \cdot P_{pulse}}{P_i^{sys}} \right), \quad (10)$$

where n_i^{sys} is the signal measured when the RF signal generator is off, P_i^{sys} is the corresponding power

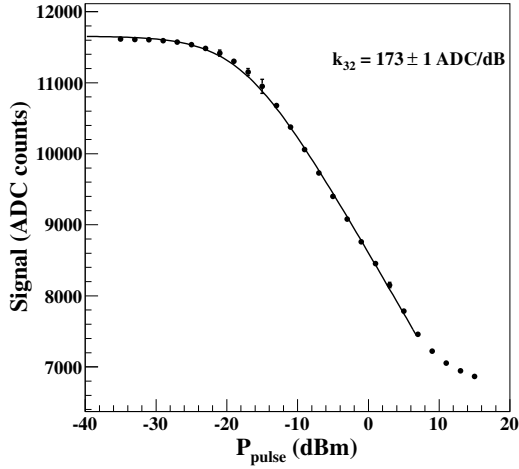


Figure 13: Example of a measurement of the calibration constant k . Closed dots represent the measured signal in pixel n. 32 for different powers of the calibration antenna pulses. The line is the result of a fit to derive k_{32} . For P_{pulse} greater than 8 dBm, measurements are affected by saturation of the LNBFs and were excluded from the fit.

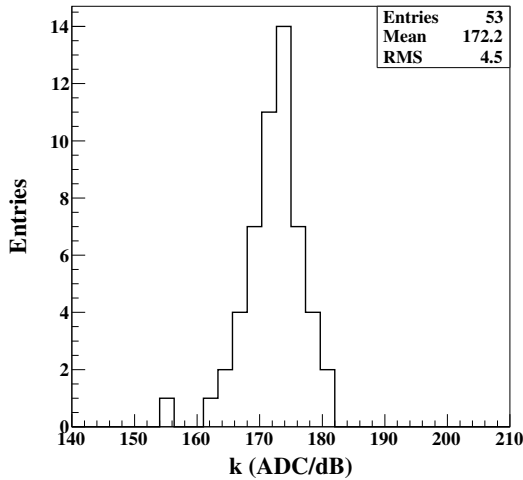


Figure 14: Distribution of the measured calibration constants k .

at the input of the power detector, and $f_i \cdot P_{pulse}$ is the power induced by the calibration pulse at the input of the power detector. The factor f_i may change from pixel to pixel, depending on the distance of the pixel from the patch antenna, on the relative orientation of the linear polarizations of the emitter antenna and the receiver, and on the signal loss L . An example of a fit of Eq. 10, with k_i , n_i^{sys} and f_i/P_i^{sys} as free parameters, to the calibra-

tion data for one channel is shown in Fig. 13. The spread of the distribution of the fitted calibration constants for the 53 channels (Fig. 14) is 2.6%, with an average of $k = 172$ ADC/dB.

The calibration pulses have a fast risetime (<1 ns) and illuminate all the camera receivers simultaneously, allowing for a measurement of their time response and synchronization. The time at which the amplitude of the measured pulse reaches 50% of its maximum value, t_{50} , was taken as an estimator. The distribution of t_{50} was found to have an RMS value of 25 ns, more than adequate for the typical pulses of microseconds duration expected from an EAS crossing the field of view of a pixel.

5. Sensitivity to EAS

The sensitivity of the MIDAS telescope to microwave emission from EAS has been studied with Monte Carlo simulations. The shower development in the atmosphere - i.e. the number of charged particles N at any given atmospheric depth - is simulated with a Gaisser-Hillas parameterization [27], including proper fluctuations of the shower profile. The shower arrival direction is isotropically distributed, with its landing point randomly distributed over a large area around the telescope. For a given shower geometry, the number of particles, $N(t)$, along the shower profile is calculated, where t is the time in 50 ns samples of the MIDAS digital electronics.

The microwave flux density at the detector aperture is then calculated, following the model in [11], as:

$$F(t) = F_{ref} \cdot \frac{\rho(t)}{\rho_0} \cdot \left(\frac{d}{R(t)} \right)^2 \cdot \left(\frac{N(t)}{N_{ref}} \right)^\alpha, \quad (11)$$

where F_{ref} is the flux density at a distance $d = 0.5$ m from a reference shower of $E_{ref} = 3.36 \times 10^{17}$ eV, $R(t)$ is the distance between the detector and the EAS segment, and $\rho(t)$ (ρ_0) is the atmospheric density at the altitude of the EAS segment (at sea level). N_{ref} is the average number of shower particles at the maximum of the EAS development for a proton primary of energy E_{ref} . The parameter α characterizes phenomenologically the coherence scaling relationship for the EAS microwave emission, with $\alpha = 2$ ($\alpha = 1$) corresponding to a fully coherent (incoherent) emission. Laboratory measurements [11] suggest a reference flux density $F_{f,ref}^0 = 1.85 \times 10^{-15}$ W/m²/Hz and full coherence at shower maximum.

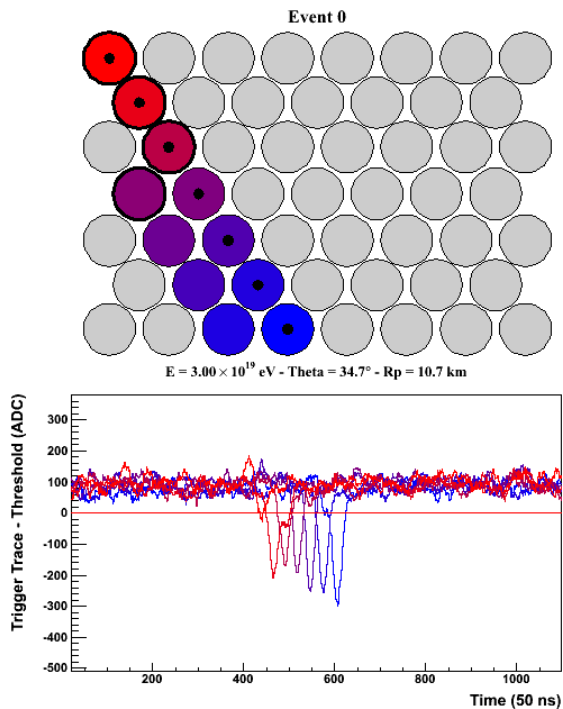


Figure 15: Event display of a $3 \cdot 10^{19}$ eV simulated shower landing approximately 10 km from the telescope. In the top panel, pixels with an FLT are highlighted, with color coded by arrival time. In the bottom panel, ADC running averages of 20 consecutive time samples for the selected pixels (identified by black dots in the top panel) are shown. The running average of each pixel is referred to the threshold level (horizontal line) for display purposes.

In order to convert the microwave flux density at the detector aperture into a signal in ADC counts, the efficiency maps and calibration constants described in Sec. 3 and Sec. 4 were implemented in the simulation. For each channel, the actual value of n_{sys} and its fluctuation were taken to be equal to their average values measured during several months of data taking, providing a realistic simulation of the telescope sensitivity. The FLT and SLT algorithms of Sec. 2.4 were also implemented, and all simulated events fulfilling the SLT condition are written to disk in the same format as the data. An example of event simulated with $F_{ref} = F_{ref}^0$ and $\alpha = 1$ is shown in Fig. 15.

Simulations with different assumptions on the characteristics of the microwave emission from EAS were performed. For $F_{ref} = F_{ref}^0$ and $\alpha = 2$, a rate of ~ 450 triggered events/year is expected, which reduces to ~ 30 events/year for $\alpha = 1$. The energy

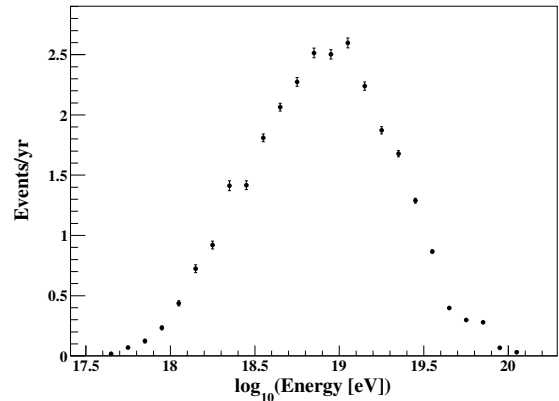


Figure 16: Expected number of triggered events per year as a function of energy, from a realistic simulation of the MIDAS telescope. A microwave flux density $F_{ref} = F_{ref}^0$ and a coherence parameter $\alpha = 1$ were used to parameterize the EAS microwave emission in the simulation.

spectrum of the triggered events is shown in Fig. 16 for the latter case.

6. Data taking performance

The MIDAS telescope underwent an extensive period of commissioning during several months in 2011 at the University of Chicago, which provided a validation of the overall design and a test of the performance and duty cycle of the detector in a particularly challenging environment for RF interference. As a matter of fact, trigger rates were found to be significantly higher than those expected from random fluctuations. The SLT rate due to accidental triggers, r_{bkg} , is estimated to be 0.3 mHz:

$$r_{bkg} = N_{patt} \cdot n_{pix} \cdot (r_{FLT})^{n_{pix}} (\tau)^{n_{pix}-1}, \quad (12)$$

where $N_{patt} = 767$ is the number of SLT patterns, $n_{pix} = 53$ is the number of pixels in the MIDAS camera, $r_{FLT} = 100$ Hz is the pixel FLT rate, and $\tau = 10 \mu s$ is the coincidence time window.

The background rate of SLT events during data taking was well above the estimate of Eq. 12 and highly variable, ranging from 0.01 Hz to 2 kHz.

The major source of background was found to originate from airplanes passing over the antenna on their way to a close-by airport. Radar altimeters on board of these aircrafts operate just above the C-Band frequency, and, while suppressed by the MIDAS receiver bandwidth, their emissions are strong enough to produce a sudden rise of the RF background in many neighboring channels (or even in

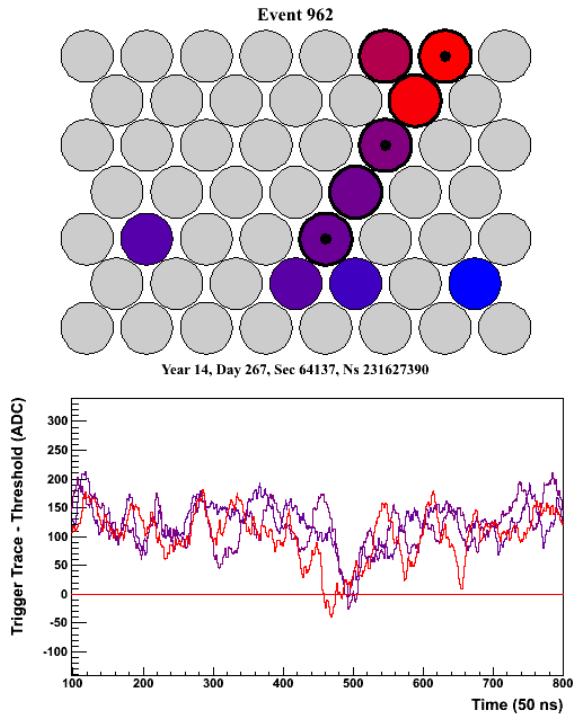


Figure 17: Event display of a candidate detected by the MIDAS telescope. See caption of Fig. 15 for a description of each panel. Although the timing characteristics of the event are compatible with those of a cosmic ray shower, correlated signals in off-track pixels do not allow for unambiguous identification.

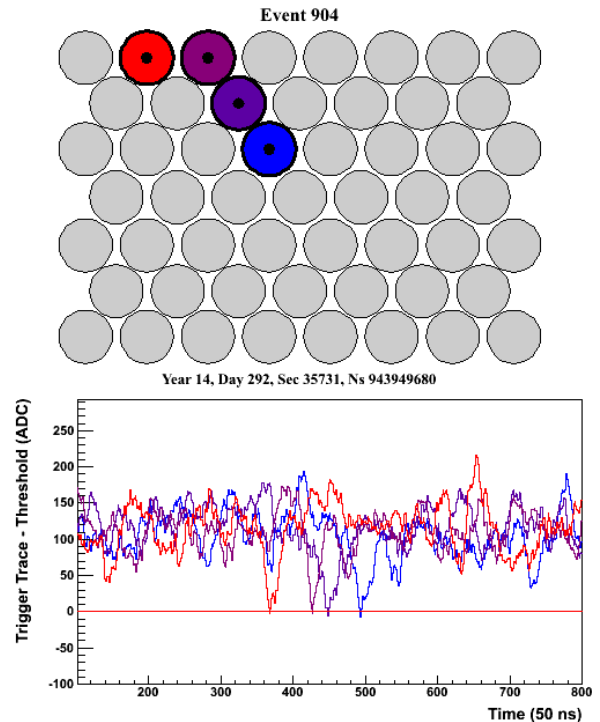


Figure 18: Event display of a 4-pixel candidate detected by the MIDAS telescope. See caption of Fig. 15 for a description of each panel. Several candidates with similar characteristics - small signals and short tracks - were found in the data.

578 the whole camera), with a corresponding increase
 579 of the first and second level trigger rates over several
 580 tens of seconds.

581 Most of the remaining background was characterized
 582 by very fast (<200 ns) transient RF signals, which
 583 trigger simultaneously from a few pixels up to the entire
 584 camera. The frequency of these events varied greatly
 585 during the data taking period, with no particular
 586 correlation with day/night or week/weekend cycles.
 587 While their exact origin was not clear, they were
 588 likely to have an anthropogenic origin in the vicinity
 589 of the detector.

590 In the early stage of commissioning, a simple
 591 veto, which inhibited the trigger system whenever
 592 the SLT rate exceeded a given value, was implemented
 593 in the FADC firmware to avoid flooding the DAQ with
 594 background events. Under this running conditions,
 595 the average live time of the detector was 60%. A
 596 significant improvement was achieved with the
 597 installation of a bandpass filter designed to reject
 598 the radar frequency band, which increased the

599 effective duty cycle of the MIDAS telescope to
 600 better than 95%.

601 The MIDAS telescope experienced very different
 602 weather conditions in Chicago - from high temperatures
 603 during summer, to heavy rain and storms, to snow
 604 and ice. Detector operation and data taking, as well
 605 as the telescope sensitivity, were found to be
 606 remarkably stable during the entire period of
 607 commissioning.

608 The main objectives of the MIDAS telescope at
 609 the University of Chicago - to validate the telescope
 610 design, and to demonstrate of a large detector
 611 duty cycle - were successfully accomplished. In
 612 addition, a first search for events compatible with
 613 EAS was performed. Examples of candidates are
 614 shown in Figs. 17 and 18. However, the characteristics
 615 of these events, which have signals close to the
 616 trigger threshold, are also compatible with a tail
 617 of the overwhelming background noise. No strong
 618 conclusion can be drawn on the origin of these
 619 events until a coincident detection with well-
 620 established techniques - for example at the Pierre
 621 Auger Observatory - is performed. A detailed
 account of the

622 search and corresponding limits on microwave emis- 669
623 sion from EAS are given in [28]. 670

624 7. Summary and conclusions

625 The MIDAS telescope - a prototype of an imag- 672
626 ing detector for microwave emission from EAS - has 673
627 been built and successfully operated at the Univer- 674
628 sity of Chicago. The telescope's design is based 675
629 on inexpensive off-the-shelf microwave components, 676
630 and a custom-made digital electronics and trigger 677
631 system. The absolute calibration of the detector 678
632 was established with measurements of the Sun and 679
633 other astrophysical objects as calibrated sources of 680
634 microwave radiation. The sensitivity over the fo- 681
635 cal plane was determined with an EM simulation 682
636 of the telescope validated by measurements of the 683
637 Sun transit in the telescope's field of view. The 684
638 sensitivity of the MIDAS detector to EAS has been 685
639 studied with Monte Carlo simulations which include 686
640 a realistic parameterization of the detector based 687
641 on these calibration measurements. Several tens to 688
642 several hundreds of events per year are expected for 689
643 microwave flux intensities as suggested by labora- 690
644 tory measurements [11]. 691

645 Several months of data taking in Chicago demon- 692
646 strated that MIDAS can be reliably operated with 693
647 minimal maintenance, and reach a duty cycle close 694
648 to 100% even in an environment with high levels of 695
649 RF background noise. Performances are expected 696
650 to further improve in the radio quiet environment of 697
651 the Pierre Auger Observatory, where MIDAS mea- 698
652 surements in coincidence with the FD and SD will 699
653 be essential to demonstrate the potential of this 700
654 novel detection technique of UHECRs. 701

655 Acknowledgments

656 This work was supported in part by the Kavli 714
657 Institute for Cosmological Physics at the Univer- 715
658 sity of Chicago through grants NSF PHY-0114422 716
659 and NSF PHY-0551142 and an endowment from the 717
660 Kavli Foundation and its founder Fred Kavli; by 718
661 the Conselho Nacional de Desenvolvimento Cient- 719
662 fico e Tecnol6gico (CNPq), Brasil; by Xunta de Gali- 720
663 cia (INCITE09 206 336 PR), Ministerio de Edu- 721
664 caci3n, Cultura y Deporte (FPA 201018410), AS- 722
665 PERA (PRI-PIMASP-2011-1154) and Consolider 723
666 CPAN Ingenio2010, Spain. The simulations used 724
667 in this work have been performed on the Joint Fer- 725
668 milab - KICP Supercomputing Cluster, supported 726
727
728
729

by grants from Fermilab, Kavli Institute for Cos-
mological Physics, and the University of Chicago.

671 References

672 References

- [1] A. Letessier-Selvon and T. Stanev, *Rev. Mod. Phys.* **83**, 907 (2011) [arXiv:1103.0031 [astro-ph.HE]].
- [2] J. Abraham *et al.* [Pierre Auger Collaboration], *Nucl. Instrum. Meth. A* **523**, 50 (2004).
- [3] T. Abu-Zayyad *et al.*, *Nucl. Instrum. Meth. A* **450**, 253 (2000).
- [4] R. U. Abbasi *et al.* [HiRes Collaboration], *Phys. Rev. Lett.* **100**, 101101 (2008) [astro-ph/0703099].
- [5] J. Abraham *et al.* [Pierre Auger Collaboration], *Phys. Rev. Lett.* **101**, 061101 (2008) [arXiv:0806.4302 [astro-ph]].
- [6] H. Falcke *et al.* [LOPES Collaboration], *Nature* **435**, 313 (2005) [astro-ph/0505383].
- [7] D. Ardouin *et al.*, *Nucl. Instrum. Meth. A* **555**, 148 (2005).
- [8] S. Fliescher [Pierre Auger Collaboration], *Nucl. Instrum. Meth. A* **662**, S124 (2012).
- [9] J. V. Jelley *et al.*, *Nuovo Cim. A* **46**, 649 (2008).
- [10] W. N. Charman and J. V. Jelley *Nuovo Cim. B* **63**, 473 (2008).
- [11] P. W. Gorham *et al.*, *Phys. Rev. D* **78**, 032007 (2008) [arXiv:0705.2589 [astro-ph]].
- [12] R. M. Baltrusaitis *et al.*, *Nucl. Instrum. Meth. A* **240**, 410 (1985).
- [13] J. Abraham *et al.* [Pierre Auger Collaboration], *Nucl. Instrum. Meth. A* **620**, 227 (2010) [arXiv:0907.4282 [astro-ph.IM]].
- [14] H. Tokuno *et al.*, arXiv:1201.0002 [astro-ph.IM].
- [15] P. Allison [Pierre Auger Collaboration], in Proc. 32nd International Cosmic Ray Conference (ICRC 2011). arXiv:1107.4807 [astro-ph.IM].
P. Facal San Luis [Pierre Auger Collaboration], to appear in Proc. of the Int. Symposium on Future Directions in UHECR Physics, 2012.
- [16] R. Smida *et al.* [CROME Collaboration], in Proc. 32nd International Cosmic Ray Conference (ICRC 2011). arXiv:1108.0588 [hep-ex]. R. Smida *et al.* [CROME Collaboration], to appear in Proc. of the Int. Symposium on Future Directions in UHECR Physics, 2012.
- [17] M. Monasor *et al.*, Proc. of the 32nd Int. Cosmic Ray Conf. (Beijing) 2011, arXiv:1108.6321; C. Williams *et al.*, to appear in Proc. of the Int. Symposium on Future Directions in UHECR Phys. (CERN) 2012.
- [18] V. Verzi *et al.*, to appear in Proc. of the Int. Symposium on Future Directions in UHECR Phys. (CERN) 2012.
- [19] M. Bogden *et al.*, Proc. of the IEEE Nuclear Science Symposium and Medical Imaging Conf. (Valencia) 2011.
- [20] R. Brun and F. Rademakers, *Nucl. Instrum. Meth. A* **389**, 81 (1997).
- [21] J. D. Kraus and R. J. Marhefka, "Antennas for All Applications," 3rd ed., McGraw-Hill, 2003.
- [22] S. J. Orfanidis, "Electromagnetic Waves and Antennas," Rutgers University, NJ, 2010.
- [23] S. Silver, ed., "Microwave Antenna Theory and Design," Dover Publications Inc, New York, 1965.
- [24] <http://solar.nro.nao.ac.jp/norp/html/daily/>

- 730 [25] International Telecommunication Union Report, ITU-R
731 P.372-10, 2009.
- 732 [26] J. W. M. Baars, R. Genzel, I. I. K. Pauliny-Toth and
733 A. Witzel, *Astron. Astrophys.* **61**, 99 (1977).
- 734 [27] T. K. Gaisser and A. M. Hillas, *Proc. of the 15th Int.*
735 *Cosmic Ray Conf. (Plovdiv)* 8, 353 (1977).
- 736 [28] J. Alvarez-Muñiz *et al.*, arXiv:1205.5785 [astro-ph.HE],
737 to appear in *Phys. Rev. D*.